Original Paper

Gravity Data Imaging Using Local Wavenumber-Based Algorithm: Sustainable Development Cases Studies

Mahmoud Elhussein[1] and Zein E. Diab[1,2]

A fast effective inversion algorithm is proposed herein to interpret gravitational responses caused by mineralized/ore sources (sphere, vertical and horizontal cylinders). The algorithm relies on local wavenumber and correlation imaging techniques. The correlation factor (R) between the local wavenumber of observed gravitational field and that of computed field was calculated, and the maximum R_{max} was considered to correspond to the best true model (parameters). The proposed algorithm was applied to two theoretical examples, including an example contaminated with regional background and another multisource example. Besides, the proposed approach was used on three different real field cases for mining/ore investigation from Canada and Cuba. From the results obtained from the theoretical and real examples and by comparing the results with drilling and literature information, it was concluded that the method is effective, is applicable even for more than one source, is accurate, and does not necessitate any prior knowledge of the source shape.

INTRODUCTION

Gravity approach is one of the most applicable geophysical potential field methods in several areas. This approach can solve various geophysical issues such as in oil, gas, mineral, and ore exploration, and it can be used to map underground geological structures, earth's crust, and sedimentary basins. It can also be used to identify the location of underground cavities, and it can be used in geothermal activities, seismological research, archeological zone, and other environmental and engineering application research (Davis et al., 1957; Nettleton, 1976; Telford et al., 1990; Greene & Bresnahan, 1998; Kearey et al., 2002; Elawadi et al., 2004; Elieff & Sander, 2004; Linford, 2006; Panisova & Pasteka,

2009; Jacoby & Smilde, 2009; Padín et al., 2012; Hinze et al., 2013; Braitenberg et al., 2016; Chen et al., 2017; Essa & Elhussein, 2018; Essa et al., 2018, 2020; Kumar et al., 2018; Al-Farhan et al., 2019; Essa & Munschy, 2019).

Several techniques have been created to analyze gravity data from different structures by approximating these different source structures to simple geometric shapes (e.g., spheres and cylinders) (Mohan et al., 1986; Salem et al., 2004; Essa 2013; Singh & Biswas, 2016) and then estimating the various parameters of the sources (e.g., amplitude factor, depth, horizontal position). Among these techniques are graphical ones that rely on characteristic points, nomograms, and master curves (Siegel et al., 1957; Grant & West, 1965; Nettleton, 1976; Prakasa Rao et al., 1986; Reynolds, 1997; Kara & Kanli, 2005; Essa, 2007, 2012); Euler and Werner-deconvolution (Werner, 1953; Thompson, 1982; Stavrev, 1997; Zhang et al., 2000; Ghosh, 2016),

[1]Department of Geophysics, Faculty of Science, Cairo University, P.O. 12613 Giza, Egypt.
[2]To whom correspondence should be addressed; e-mail: zdiab@cu.edu.eg
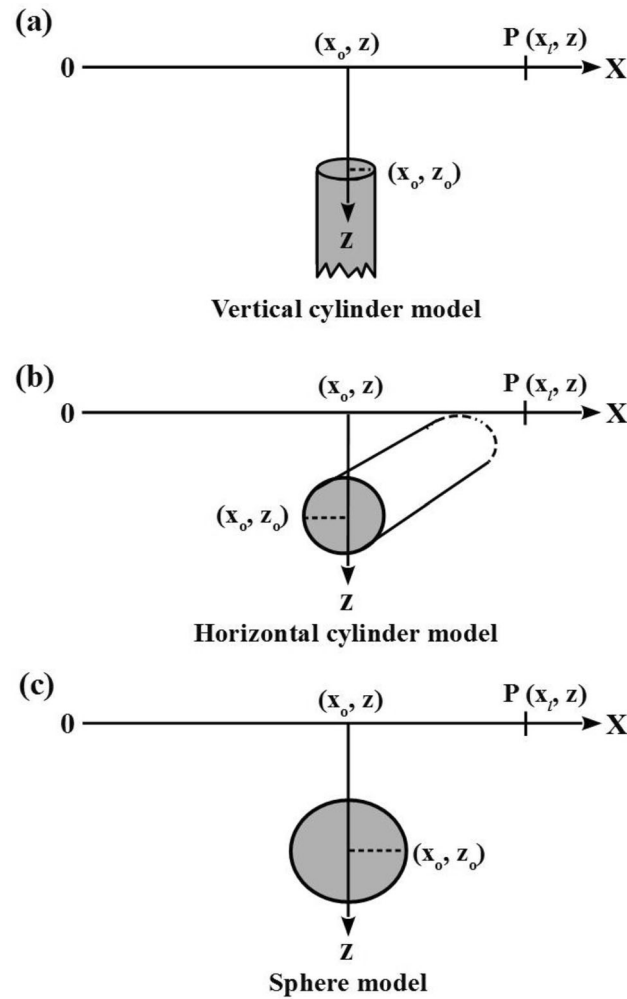
Figure 1. Schematic diagram and distribution of the different geometrical shape sources.

Table 1. Definitions of A, m, and q for source geometry shown in Figure 1; r represents the radius (m) of source body, ρ represents density contrast (gm/cm^3), and λ represents the universal gravitational constant (6.67×10^{11} m^3/kg s^2)

Source geometry	A	q	m
Vertical cylinder	$\pi\lambda\rho r^2$	0.5	0
Horizontal cylinder	$2\pi\lambda\rho r^2$	1	1
Sphere	$\frac{4}{3}\pi\lambda\rho r^3$	1.5	1

derivatives method (Saad, 2006; Essa, 2007; Ekinci et al., 2013), least squares approach (Gupta, 1983; Abdelrahman & Sharafeldin, 1995; Essa, 2011, 2014; Abdelrahman & Essa, 2015) and 2D, 2.5D, and 3D modeling (Chai & Hinze, 1988; Pinto & Casas, 1996; Zhang et al., 2001; Eshaghzadeh & Hajian, 2018). Most of these previous methods have difficulties in inversion, which include the necessity of prior information (geological information), dependence of few specific points and accuracy in regional-residual anomaly separation, and ignoring other points along a profile, resulting in ill-posed and ambiguity issues (Zhdanov, 2002; Tarantola, 2005; Essa & Munschy, 2019). These different problems lead to high uncertainty in predicted source parameters and estimated anomaly or model shift (Nettleton, 1976; Essa & Elhussein, 2018).

Nowadays, new techniques based upon artificial intelligence have been developed. For examples,
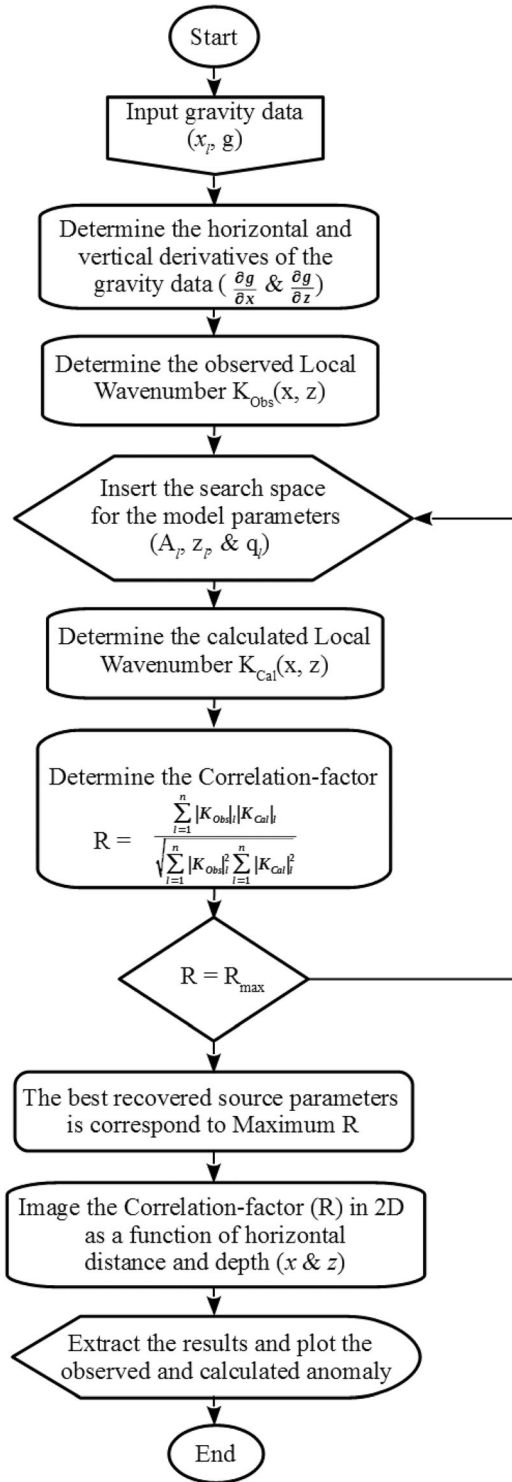
Figure 2. Flowchart illustrating the sequence procedures of the proposed algorithm.

these techniques include genetic algorithm (Amjadi & Naji, 2013; Di Maio et al., 2016, 2020; Kaftan, 2017), simulated annealing (Sen & Stoffa, 2013; Biswas et al., 2014, 2017; Biswas, 2016), particle-swarm-optimization (Toushmalani, 2013; Singh & Biswas, 2016; Essa & Munschy, 2019), and the differential evolution technique (Wu et al., 2014; Ekinci et al., 2016; Balkaya et al., 2017).

An efficient imaging algorithm was developed in this study to fully interpret gravitational data caused by various underground structures (sphere, horizontal cylinder, and vertical cylinder). This approach relies upon calculating the correlation factor (R) parameter between the local wavenumber of observed gravitational field and that of the computed field. The model that corresponds to the highest R parameter was interpreted as the best model. This approach can be used in different applications, such as mineral and ore exploration, as it determines the different structure parameters, which include amplitude factor (A), depth (h), body origin (w), and shape factor (q), and it does not necessitate any prior knowledge of the source shape. Moreover, the method can be applied to estimate multisource parameters. To confirm the efficacy and the applicability of the suggested approach, this method was used to invert gravity data of three various theoretical examples with and without 20% Gaussian noise levels and three field examples from Canada and Cuba.

METHODOLOGY

The gravitational anomaly (g) caused by different geometrical structures (vertical cylinder, sphere, and horizontal cylinder) at horizontal position (x_l, z) along a profile (Fig. 1) (Salem et al., 2004; Asfahani & Tlas, 2008; Essa, 2014; Essa et al., 2020) can be calculated as:

$$g(x_l, x_o, z, z_o, q, A) = \frac{A(z_o - z)^m}{\left[(x_l - x_o)^2 + (z_o - z)^2\right]^q}, l$$
$$= 1, 2, 3, \dots, n$$
(1)

where x_o is the location of the structure in horizontal direction, z_o is the depth of the structure, q is the shape factor, m is the exponent constant varied according to the value of q (i.e., for $q = 0.5$, $m = 0$; for $q = 1$ and 1.5, $m = 1$, as presented in Table 1),
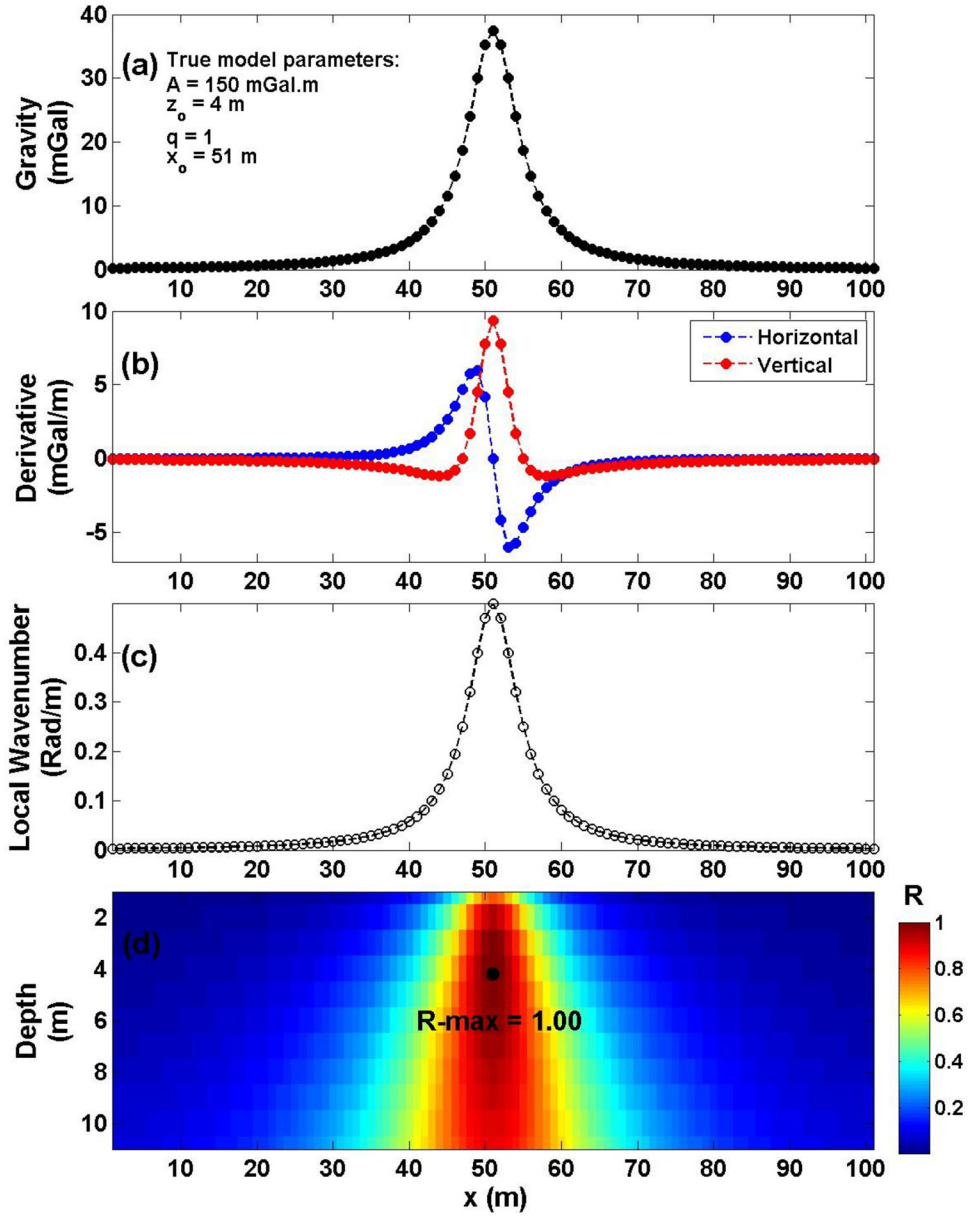
Figure 3. Model 1: (**a**) gravitational anomaly profile caused by a horizontal cylinder; (**b**) calculated horizontal and vertical derivatives for the profile displayed in (**a**); (**c**) local wavenumber of the derivatives illustrated in (b); and (d) imaging of R and the maximum R predicted from the proposed algorithm.

and A is the amplitude factor that relies upon the type of structure (Table 1).

The observed local wavenumber (K_{Obs}) can be formulated as (Ma et al., 2017):

where

$$K_{Obs} = \frac{\partial \theta}{\partial x}, \qquad (2)$$

Table 2. Maximum correlation factors (R) corresponding to the various shape factors (q)

Shape factor (q)	Maximum R
0.5	0.9883
0.6	0.9882
0.7	0.9988
0.8	0.9994
0.9	0.9986
1	**1.0000**
1.1	0.9991
1.2	0.9978
1.3	0.9991
1.4	0.9996
1.5	0.9996

Model 1: Noise-free data

Table 3. True and recovered model parameters for Model 1: noise-free example presented in Figure 2

Model parameters	True	Recovered
A (mGal.m)	150	150
z_o (m)	4	4
x_o (m)	51	51
q	1.0	1.0
Maximum R		1.0000

$$\theta = \tan^{-1}\left[\frac{\left(\frac{\partial g}{\partial z}\right)}{\left(\frac{\partial g}{\partial x}\right)}\right], \qquad (3)$$

Substituting Eq. 3 into Eq. 2, K_{Obs} can be calculated as:

$$K_{Obs} = \frac{\partial}{\partial x}\tan^{-1}\left[\frac{\left(\frac{\partial g}{\partial z}\right)}{\left(\frac{\partial g}{\partial x}\right)}\right]$$
$$= \frac{1}{AS^2}\left[\left(\frac{\partial^2 g}{\partial x \partial z}\cdot\frac{\partial g}{\partial x}\right) - \left(\frac{\partial^2 g}{\partial x^2}\cdot\frac{\partial g}{\partial z}\right)\right], \quad (4)$$

where AS represents the amplitude of the analytic signal (Nabighian, 1972):

$$AS = \sqrt{\left(\frac{\partial g}{\partial x}\right)^2 + \left(\frac{\partial g}{\partial z}\right)^2}, \qquad (5)$$

By taking the horizontal $\left(\frac{\partial g}{\partial x}\right)$ and vertical $\left(\frac{\partial g}{\partial z}\right)$ derivatives of Eq. 1 analytically, substituting them into Eq. 4, and abbreviating the resultant equation, the calculated local wavenumber (K_{Cal}) is:

$$K_{Cal} = \frac{-2q(z_o - z)[(2q - m)(z_o - z)^2 + m(x_l - x_o)^2}{\left[(2q - m)(z_o - z)^2 - m(x_l - x_o)^2\right]^2 + 4q^2z^2(x_l - x_o)^2}, \qquad (6)$$

For K_{Obs} and K_{Cal}, the correlation factor (s) can be obtained as (Ma et al., 2017):

$$R = \frac{\sum_{l=1}^{n}|K_{Obs}|_l|K_{Cal}|_l}{\sqrt{\sum_{l=1}^{n}|K_{Obs}|_l^2 \sum_{l=1}^{n}|K_{Cal}|_l^2}}. \qquad (7)$$

With Eq. 7, the R between K_{Obs} and K_{Cal} is calculated, and the maximum R corresponds to real body parameters (Ma et al., 2017). Figure 2 shows a flowchart of the sequence procedures of the proposed algorithm. Once the best optimal parameters are chosen from the search space based on the maximum R, the 2D image of the R of the preferred source (i.e., shape factor q and its related m) can be constructed as a function of the depth (m) of the subsurface. The solid black dot on the imaging section represents the correct location for depth and location.

THEORETICAL EXAMPLES

This section applies the proposed technique to three different noisy and noise-free synthetic examples to examine the efficiency and applicability of the proposed approach in interpreting gravity anomalies.

Model 1

A pure gravity profile caused by horizontal cylinder was computed using the following parameters: A = 150 mGal.m, z_o = 4 m, q = 1, x_o = 51 m, and profile length of 100 m (Fig. 3a). Interpretation began with the calculation of horizontal and vertical derivatives of the observed data (Fig. 3b), and then, K_{Obs} was calculated using Eq. 4 (Fig. 3c). Next, R was calculated by applying Eq. 7 (Fig. 3d) using different values of q (Table 2). Figure 3d shows the maximum R = 1 (black circle) located at x_o = 51 m, z_o = 4 m, and q = 1 (Table 3), indicating that the suggested method is highly efficient. The proposed method was used to estimate the inverted parameters (Table 3), and the errors of the different parameters account to 0%.
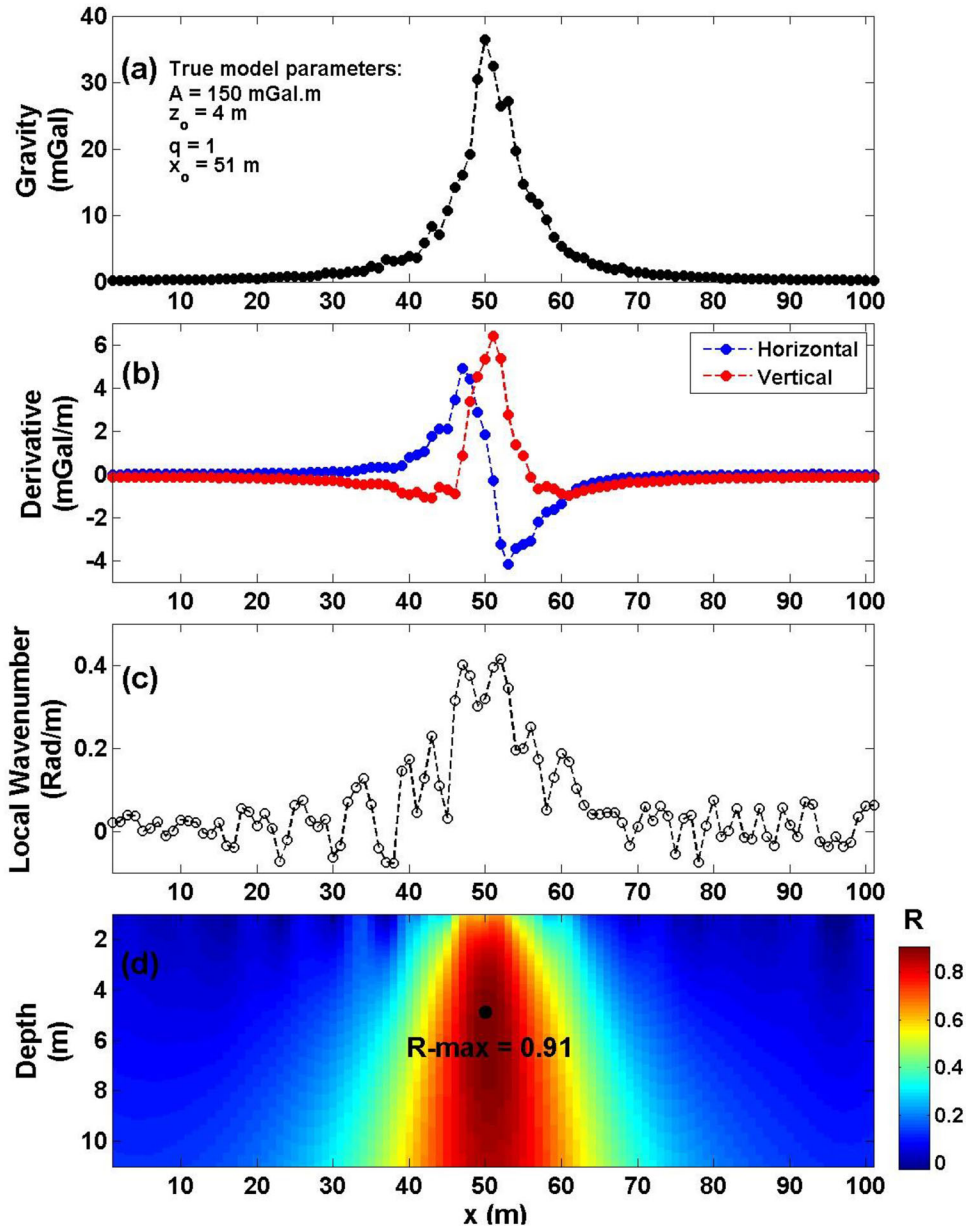
Figure 4. Model 1: (**a**) gravitational anomaly profile of Fig. 3a contaminated with 20% Gaussian random noise; (**b**) calculated horizontal and vertical derivatives for the profile displayed in (**a**); (**c**) local wavenumber of the derivatives illustrated in (**b**); (**d**) *R* image and the maximum *R* result.

To investigate the stability and the performance of the proposed approach to noisy data, a 20% Gaussian random noise was added to the previous gravity anomaly (Fig. 4a). First, the vertical and horizontal derivatives of the noisy data were calculated (Fig. 4b), and then, K_{Obs} was calculated applying Eq. 4 (Fig. 4c). Equation 7 was then applied to calculate R (Fig. 4d). Figure 4d shows the maximum $R = 0.9061$ (black circle) located at $x = 50$ m, $z = 4.7$ m, and $q = 1$ (Table 4), indicating that the suggested technique can be applied with high performance to noisy data. The proposed approach was used to estimate the inverted parameters (Table 4), and the errors of A, z_o, x_o, and q were 1.69, 17.5, 1.96, and 0%, respectively.

Table 4. True and recovered model parameters for Model 1: the noisy synthetic example presented in Figure 3

| Model parameters	True	Recovered
A (mGal.m)	150	152.54
z_o (m)	4	4.7
x_o (m)	51	50
q	1.0	1.0
Maximum R		0.9061

Model 2

In some real-world cases, multiple structures or bodies can cause gravity anomalies. Therefore, this study aimed to explore the applicability of the suggested approach in the presence of multisource models. A composite gravity anomaly was computed using a horizontal cylinder model (with the following parameters: $A = 120$ mGal.m, $z_o = 3$ m, $x_o = 30$
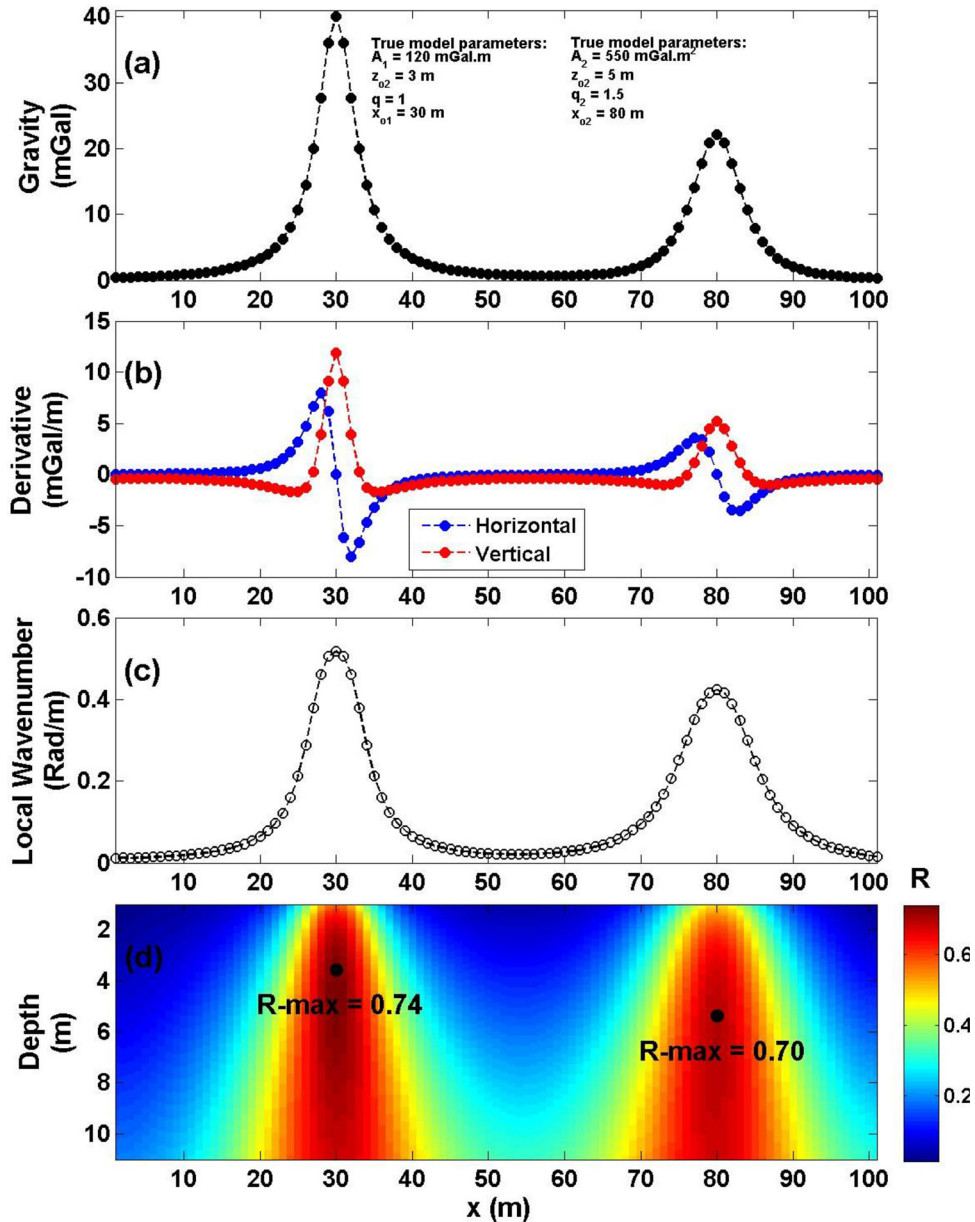
Figure 5. Model 2: (**a**) composite gravitational anomaly profile caused by two different structures; (**b**) calculated horizontal and vertical derivatives for the profile displayed in (**a**); (**c**) local wavenumber of the derivatives illustrated in (**b**); and (**d**) R image and the maximum R result.

Table 5. True and recovered model parameters for Model 2: the noise-free interfering and neighboring sources

Model parameters	True models parameters		Recovered models parameters	
	Horizontal cylinder model	Sphere model	Horizontal cylinder model	Sphere model
A (mGal.m^{2q-m})	120 mGal.m	550 mGal.m^2	122.47 mGal.m	564.62 mGal.m^2
z_o (m)	3	5	3.4	5.2
x_o (m)	30	80	30	80
q	1.0	1.5	1.0	1.5
Maximum R			0.74	0.70
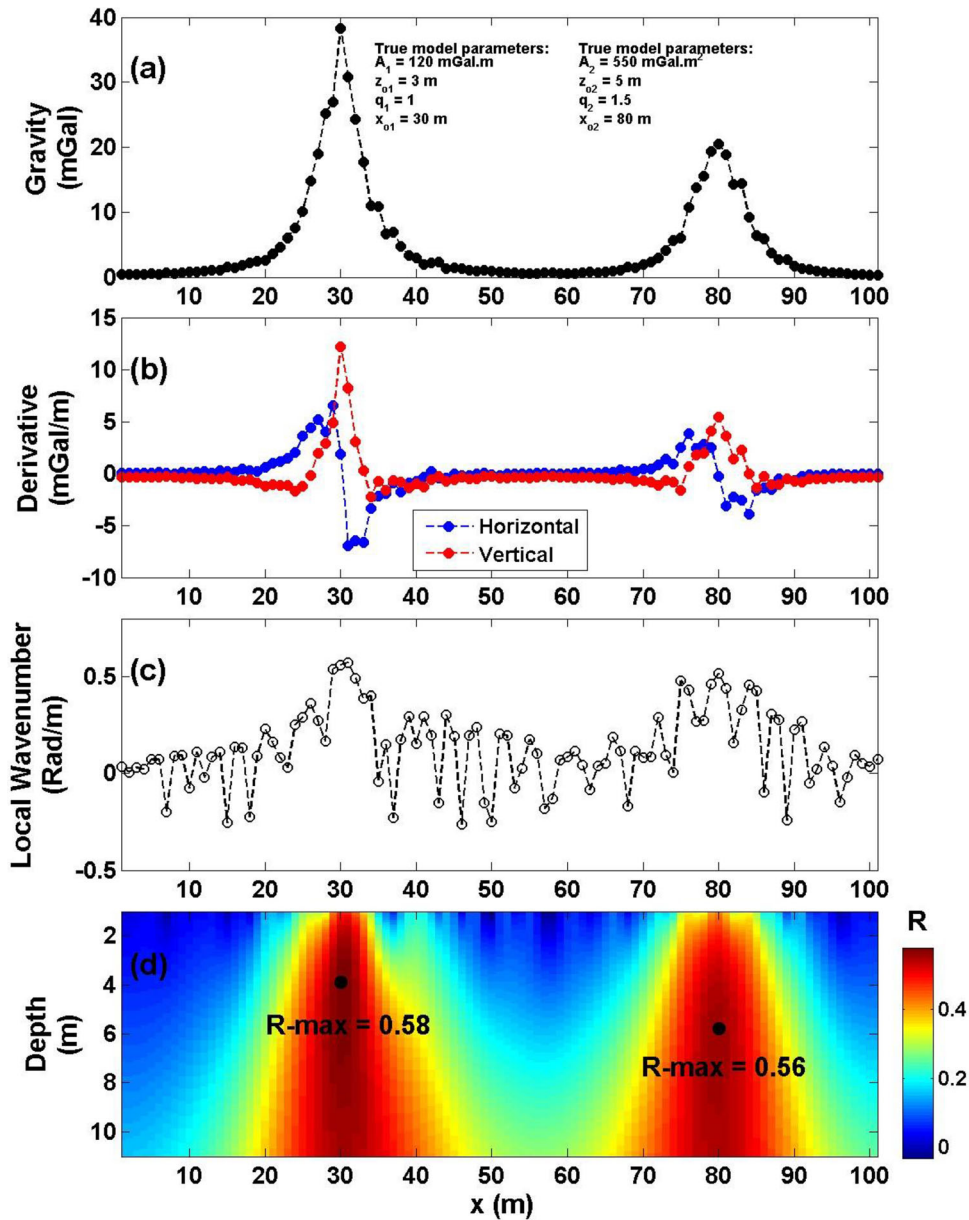
Figure 6. Model 2: (**a**) composite gravitational anomaly profile of Figure 5a contaminated with 20% Gaussian random noise; (**b**) calculated horizontal and vertical derivatives for the profile displayed in (**a**); (**c**) local wavenumber of the derivatives illustrated in (**b**); and (**d**) R image and the maximum R result.

Table 6. True and recovered model parameters for Model 2: the noisy contaminated interfering and neighboring sources after adding 20% Gaussian random noise to the free-noise model

Model parameters	True models parameters		Recovered models parameters	
	Horizontal cylinder model	Sphere model	Horizontal cylinder model	Sphere model
A (mGal.m^{2q-m})	120 mGal.m	550 mGal.m^2	113.75 mGal.m	591.67 mGal.m^2
z_o (m)	3	5	3.7	5.6
x_o (m)	30	80	30	80
q	1.0	1.5	1.0	1.5
Maximum R			0.58	0.56

m, and $q = 1$) and a sphere model (with the following parameters: $A = 550$ mGal.m^2, $z_o = 5$ m, $x_o = 80$ m, and $q = 1.5$) (Fig. 5a). Interpretation began by calculating the vertical and horizontal derivatives of the observed composite profile (Fig. 5b). The K_{Obs} was calculated using Eq. 4 (Fig. 5c), and the R was calculated using Eq. 7 (Fig. 5d). Figure 5d shows the maximum R of the first body to be 0.74 (first black circle) located at $x_o = 30$ m, $z_o = 3.4$ m, and $q = 1$ and the maximum R of the second body to be 0.70 (second black circle) located at $x_o = 80$ m, $z_o = 5.2$ m, and $q = 1.5$ (Table 5). The errors of A, z_o, x_o, and q were 2.06, 13.33, 0, and 0%, respectively, for the horizontal cylinder structure, while the errors of A, z_o, x_o, and q were 2.66, 4, 0, and 0%, respectively, for the spherical structure.

To use the suggested approach in the presence of noisy data, a 20% Gaussian random noise was added to the previous composite gravity anomaly (Fig. 6a). First, the vertical and horizontal derivatives of the noisy composite profile were calculated (Fig. 6b), the K_{Obs} was computed (Fig. 6c), and R was calculated (Fig. 6d). Figure 6d shows the maximum R of the first body to be 0.58 (first black circle) located at $x_o = 30$ m, $z_o = 3.7$ m, and $q = 1$ and the maximum R of the second body to be 0.56 (second black circle) located at $x_o = 80$ m and $z_o = 5.6$ m, and $q = 1.5$ (Table 6). The errors of A, z_o, x_o, and q were 5.21%, 23.33%, 0%, and 0%, respectively, for the horizontal cylinder structure, while the errors of A, z_o, x_o, and q were 7.58, 12, 0, and 0%, respectively, for the spherical structure.

Thus, it can be concluded that the proposed method is highly applicable in multisource cases.
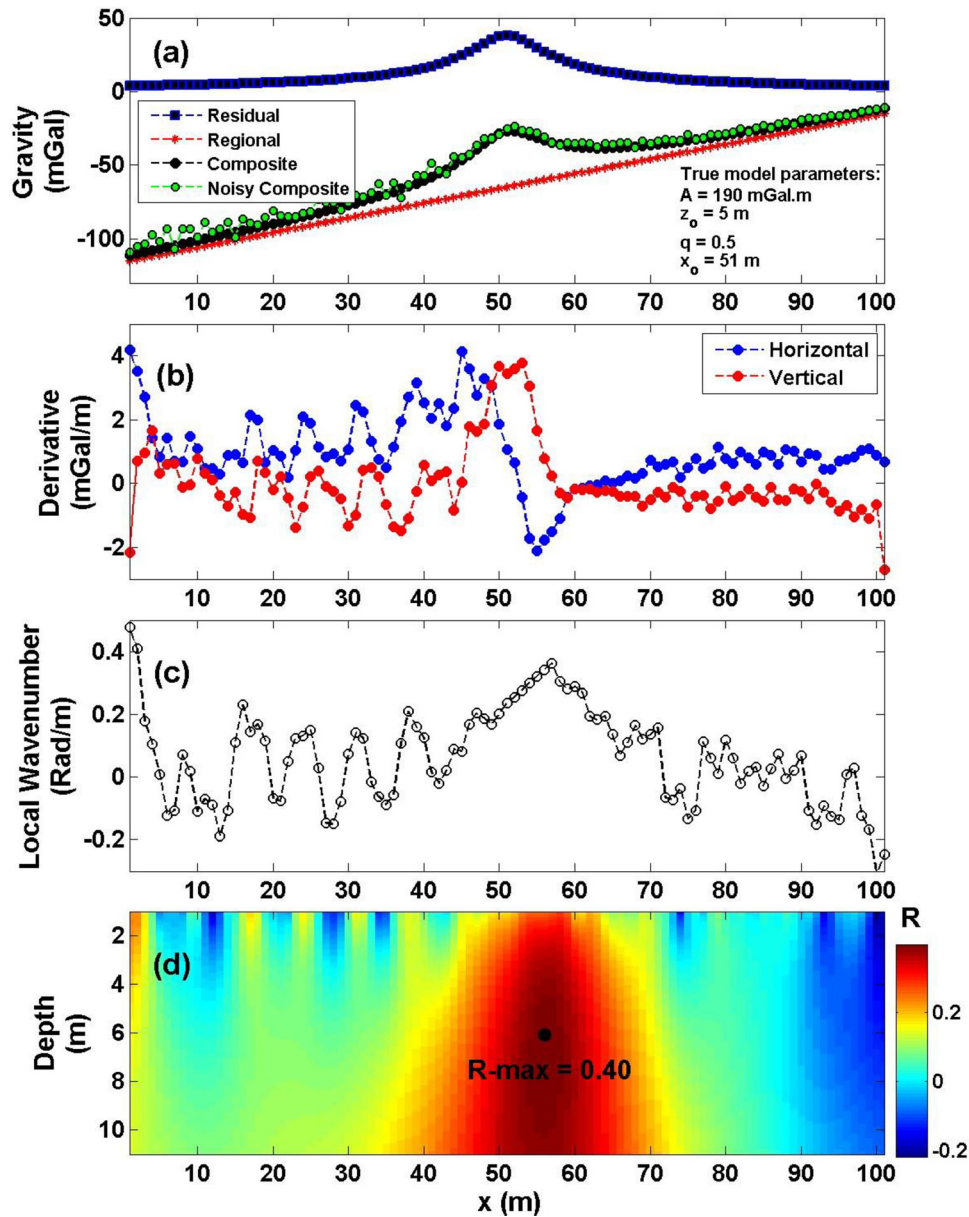
Model 3

The effectiveness of the proposed technique in the presence of regional anomaly was studied. Regional anomaly (first order) was computed, and a composite gravity anomaly consisting of vertical cylinder was computed using the following parameters: $A = 190$ mGal.m, $z_o = 5$ m, $x_o = 51$ m, and $q = 0.5$. Moreover, a 10% Gaussian random noise was added (Fig. 7a). Using the same procedure mentioned above, the vertical and horizontal derivatives of the observed composite profile were computed (Fig. 7b). The K_{Obs} (Fig. 7c) and the R were then calculated (Fig. 7d). Figure 7d shows the maximum R to be 0.40 (black circle) located at $x_o = 56$ m, $z_o = 5.9$ m, and $q = 0.5$ (Table 7). The errors of A, z_o, x_o, and q were 9.56, 18, 9.80, and 0%, respectively. The results so far show the effectiveness of the proposed technique even if the data were contaminated with regional background.

FIELD EXAMPLES

To test the performance of the proposed approach, it was applied to three different real cases, one from Cuba and two from Canada.

Mobrun Anomaly, Québec, Canada

The Mobrun area is situated about 34 km northeast of Rouyn-Noranda (Barrett et al., 1992) (Fig. 8). It is underlain by the Renault Formation, which is lined with Destor rocks from north to south.

Figure 7. Model 3: (**a**) composite gravitational anomaly profile of a vertical cylinder model and regional background (first order) after adding 10% Gaussian random noise; (**b**) calculated horizontal and vertical derivatives for the profile displayed in (**a**); (**c**) local wavenumber of the derivatives illustrated in (**b**); and (**d**) *R* image and the maximum *R* result.

The Renault Formation consists of large fragmental rhyolitic and andesitic units (Barrett et al., 1992). The footwall of the Mobrun area is composed of Copper Hill rhyolite unit, which is underlain by an andesitic–rhyolite and andesite sequence followed by a level of felsic pyroclastic rocks, while the hanging wall is composed of massive rhyolite that similarly correlates to the footwall stratigraphy of the main complex along the strike to the west. Brecciated rhyolite is present immediately beneath

Table 7. True and recovered model parameters for Model 3: the noisy composite gravity anomaly (residual gravity anomaly of vertical cylinder model + first-order regional effect) using 10% Gaussian random noise

Model parameters	True	Recovered
A (mGal.m)	190	208.16
z_o (m)	5	5.9
x_o (m)	51	56
q	0.5	0.5
Maximum R		0.40

the main complex (Caumartin & Caill, 1990; Barrett et al., 1992). The Mobrun deposit is made up of two enormous sulfide lens complexes. The main complex is made up of five ore bodies.

Figure 9 shows the residual gravity map over the Mobrun ore. A profile was extracted from the residual gravity map, and this profile was taken perpendicular to the massive sulfide body (Grant & West, 1965; Sivakumar Sinha, & Ram Babu, 1985; Roy et al., 2000; Biswas, 2015) (Fig. 10a). The gravity profile was 230 m long, and it was sampled at 2 m intervals. The gravity profile was subjected to the local wavenumber approach by computing the
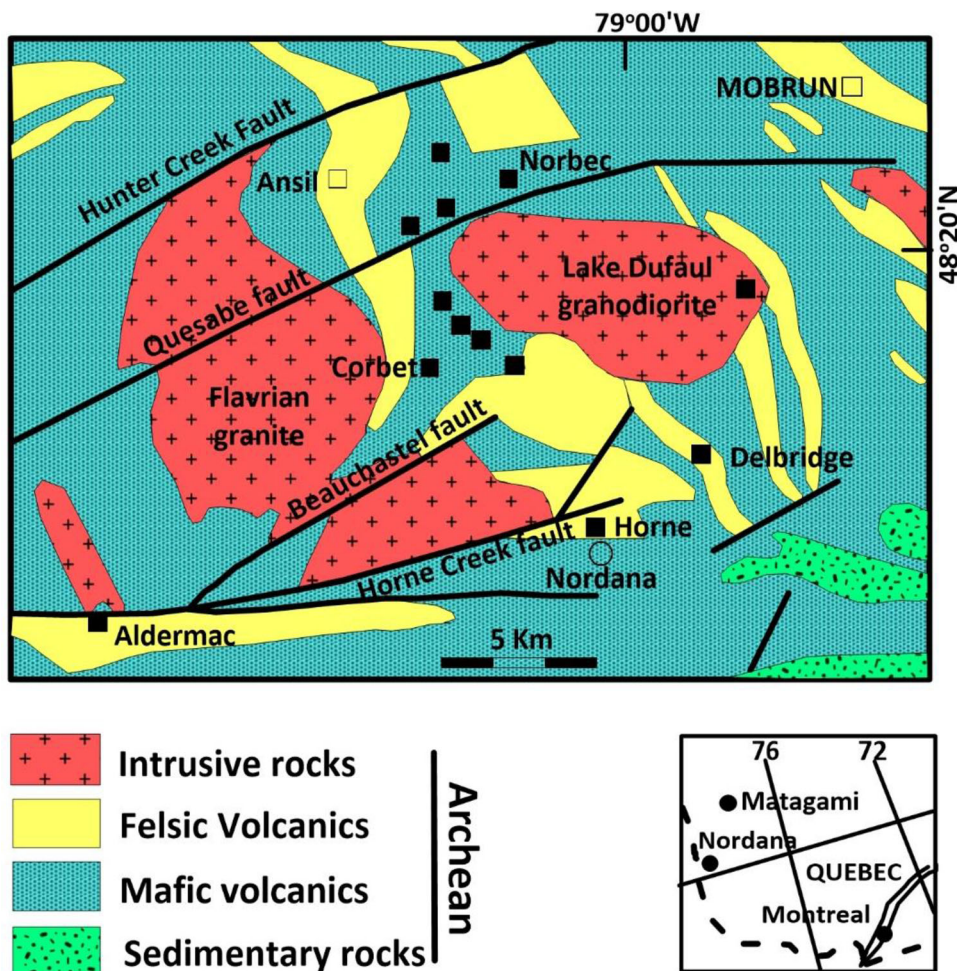
Figure 8. Geological map of the Noranda property, Canada (after Barrett et al., 1992). Open squares represent currently producing mines; closed ones represent past mines.
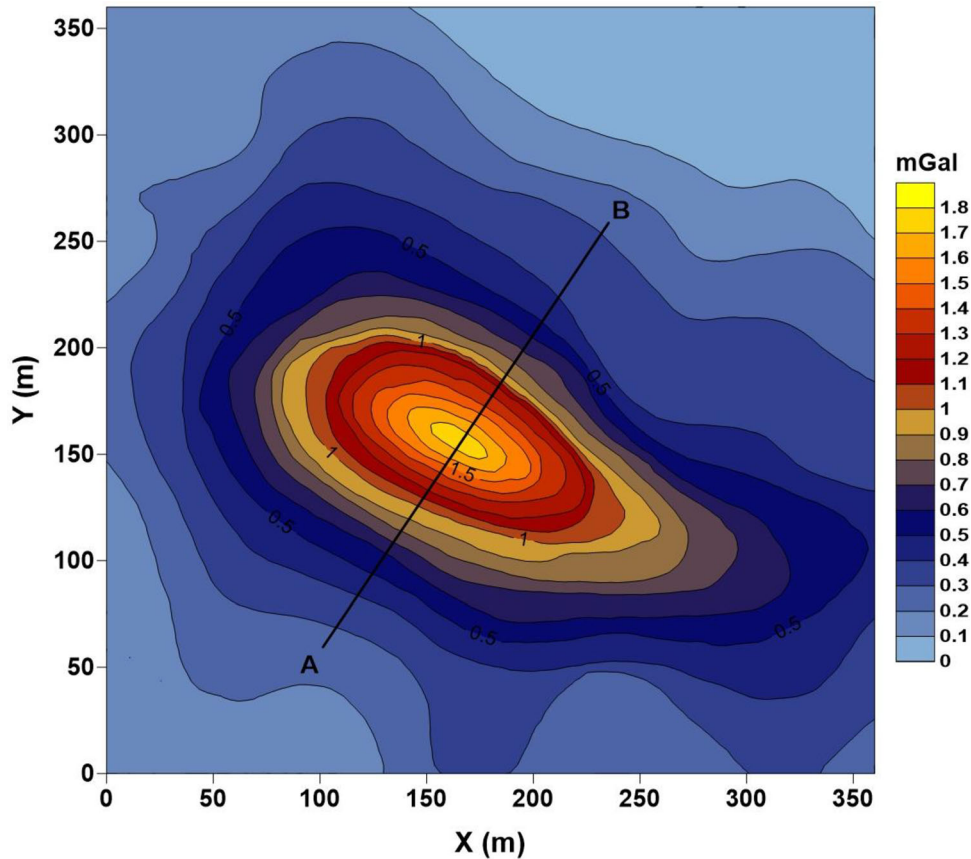
Figure 9. The Mobrun anomaly, Canada. Residual gravity anomaly map (Ekinci et al., 2016). AB denotes the gravity anomaly profile (Fig. 10) subjected to interpretation.
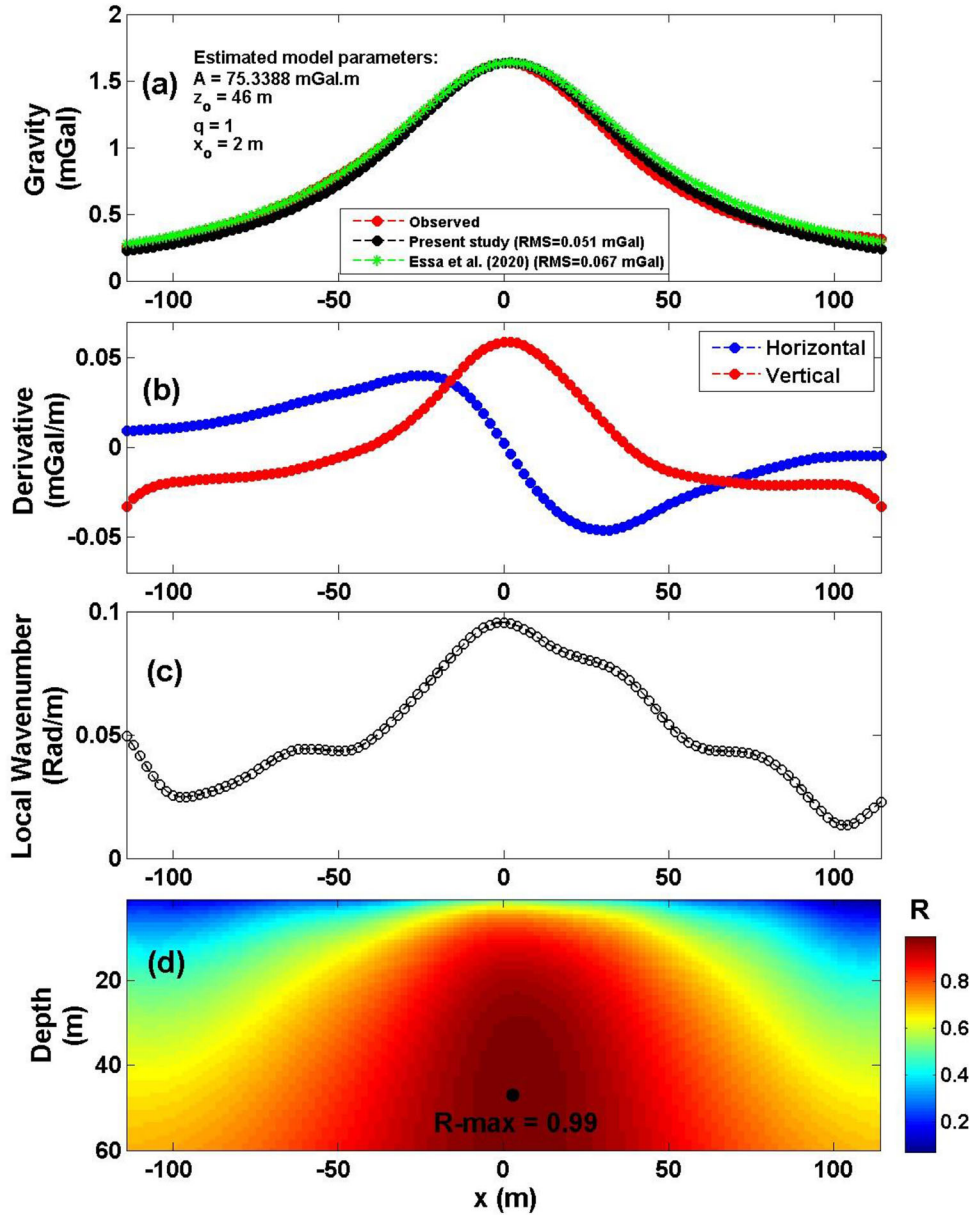
horizontal and vertical derivatives (Fig. 10b), followed by computing the K_{Obs} (Fig. 10c). The R was then calculated (Fig. 10d) using different values of q (Table 8). Figure 10d shows the maximum R to be 0.99 (black circle) located at $x_o = 2$ m, $z_o = 46$ m, and $q = 1$ (Table 9). Table 9 summarizes the predicted structure parameters, indicating that the body is a horizontal cylinder. Figure 10a shows a comparison between the observed and the inverted gravity profiles, which have an excellent coincidence. Figure 10a also shows that the present approach had less RMS error between the observed and calculated anomaly than was obtained by other techniques (Essa et al., 2020). Table 9 presents the comparison between the inverted parameters of the proposed method and those of the various methods in the literature.

Camaguey Chromite Anomaly, Cuba

The Camaguey chromite deposits formed at the intersection of serpentinized dunite and peridotite rocks and feldspathic rocks (Davis et al., 1957) (Fig. 11). Davis et al. (1957) collected chromite gravity data throughout a dipping sheet-shaped chromite-bearing ore deposit in the Camaguey District of Cuba as part of a United States Geological Survey exploration expedition.

Figure 12 illustrates the gravity map over the Camaguey chromite deposits. A profile was extracted from the residual gravity map and was taken perpendicular to the strike of the chromite deposit (Fig. 13a). The gravity profile length is 89 m and was sampled at 2 m intervals. The local wavenumber approach was applied to the gravity profile by

Figure 10. The Mobrun anomaly, Canada. (**a**) Gravity anomaly profile (red dotted lines) and the best-fitting model (solid black line). (**b**) Horizontal and vertical derivatives of the data shown in (**a**). (**c**) Local wavenumber of the data presented in (**b**). (**d**) R image (maximum $R = 0.99$).

computing the horizontal and vertical derivatives (Fig. 13b), followed by computing the K_{Obs} (Fig. 13c). After that, the R was calculated (Fig. 13d) using different values of q (Table 10). Figure 13d shows the maximum R to be 0.97 (black

circle) located at $x_o = -2$ m, $z_o = 15$ m, and $q = 1$ (Table 11). Table 11 presents the predicted parameters, indicating that the body is a horizontal cylinder. Figure 13a shows the comparison between the observed and the inverted gravity profiles, which are

Table 8. Maximum R for the various shape factors of the Mobrun gravity anomaly, Canada

| Shape factor (q)	Maximum R
0.5	0.992591
0.6	0.992591
0.7	0.993779
0.8	0.993818
0.9	0.993836
1	**0.993837**
1.1	0.993820
1.2	0.993793
1.3	0.993763
1.4	0.993723
1.5	0.993683

Bold refers to the maximum value overall R

closely matched. In addition, Figure 13a also shows that the present approach had less RMS error between the observed and calculated anomaly than was obtained by other techniques (Essa et al., 2020). The depth obtained from the proposed method matched well with the drilling information (Fig. 14). Table 10 presents the comparison between the inverted parameters of the proposed method and those from different techniques in the literature.

Faro Gravity Anomaly, Yukon, Canada

Faro Mine lies 15 km north of Faro in the south-central Yukon Territory of Northern Canada.

Table 9. The recovered parameters for the Mobrun gravity anomaly, Canada, and the comparison results with the published studies

Model parameters	Mehanee (2014)	Biswas (2015)	Singh and Biswas (2016)	Essa et al. (2020)	Present study
A (mGal.m)	80	79.5	–	38.47	75.33
z_o (m)	47	47.7	46.69	47	46
q	1	1	1	0.91	1
x_o (m)	–	2.5	2.37	2	2
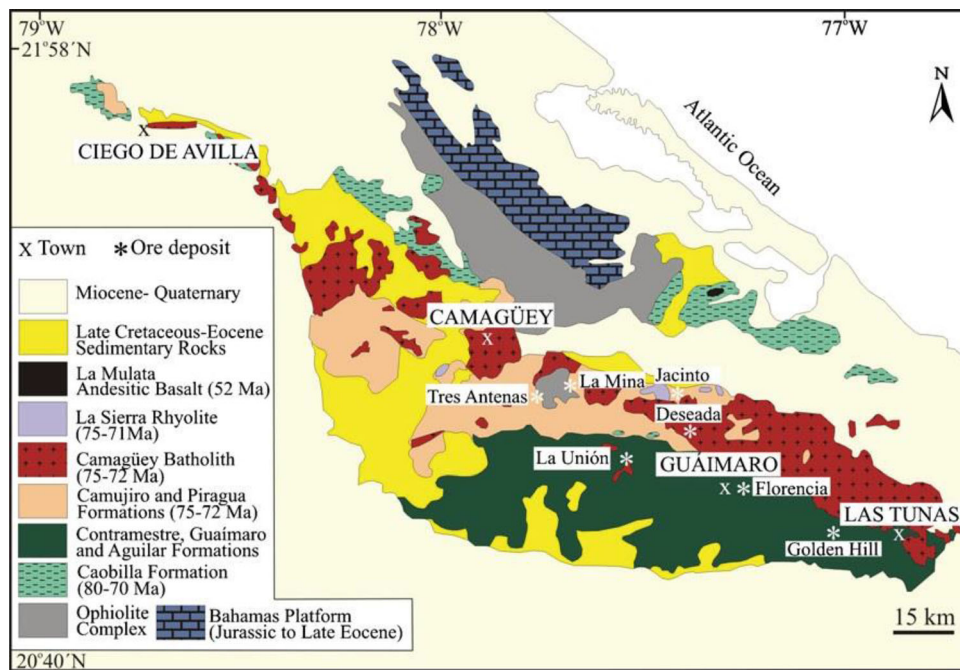
**Figure 11.** Location and geology of the Camaguey District (from Santana et al., 2011).
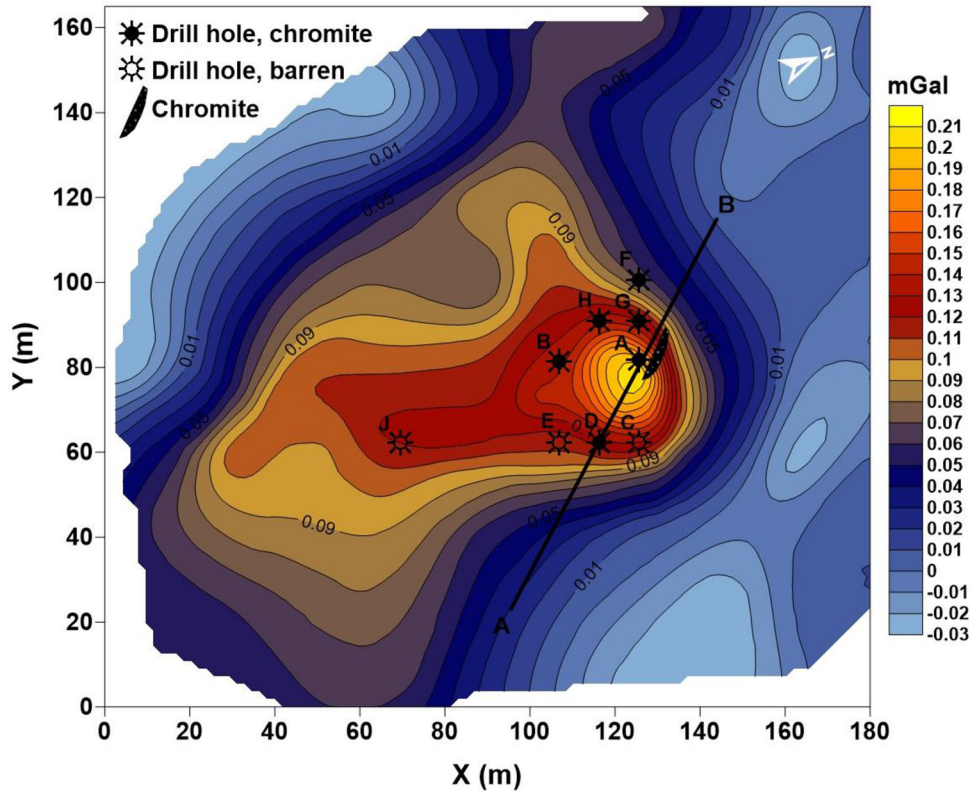
Figure 12. The Camaguey anomaly, Cuba. Residual gravity anomaly map (Davis et al., 1957; Roy, 2001). AB denotes the gravity anomaly profile (Fig. 13) subjected to interpretation.

It is located in the northwest area of the Faro Complex (Tang, 2011) (Fig. 15). The geography of the property is dictated by the Yukon Plateau and the adjacent mountains of Anvil Range, with altitudes above 1800 m. The regional geology of the Faro Mine can be illustrated by the Anvil district geology (Tang, 2011) (Fig. 16).

Figure 17a shows the residual gravity profile above the Faro mine. Figure 17b displays the geological cross section of the profile. The profile length was 805 m and was sampled at 12 m intervals (Fig. 18a). The local wavenumber approach was applied to the gravity profile by computing the horizontal and vertical derivatives (Fig. 18b), followed by computing the K_{Obs} (Fig. 18c). After that, the R was calculated (Fig. 18d) using different val-

ues of q (Table 12). Figure 18d shows the maximum R to be 0.99 (black circle) located at $x_o = 378$ m, $z_o = 290$ m, and $q = 1.5$ (Table 13). Table 13 presents the inverted parameters, indicating that the body is a sphere. Figure 18a shows the comparison between the observed and the inverted gravity profiles, with relatively good matching. In addition, Figure 18a also shows that the present approach had less RMS error between the observed and calculated anomaly than was obtained by other techniques (Essa et al., 2020). Table 13 presents the comparison between the inverted parameters of the proposed method and those from different techniques in the literature.
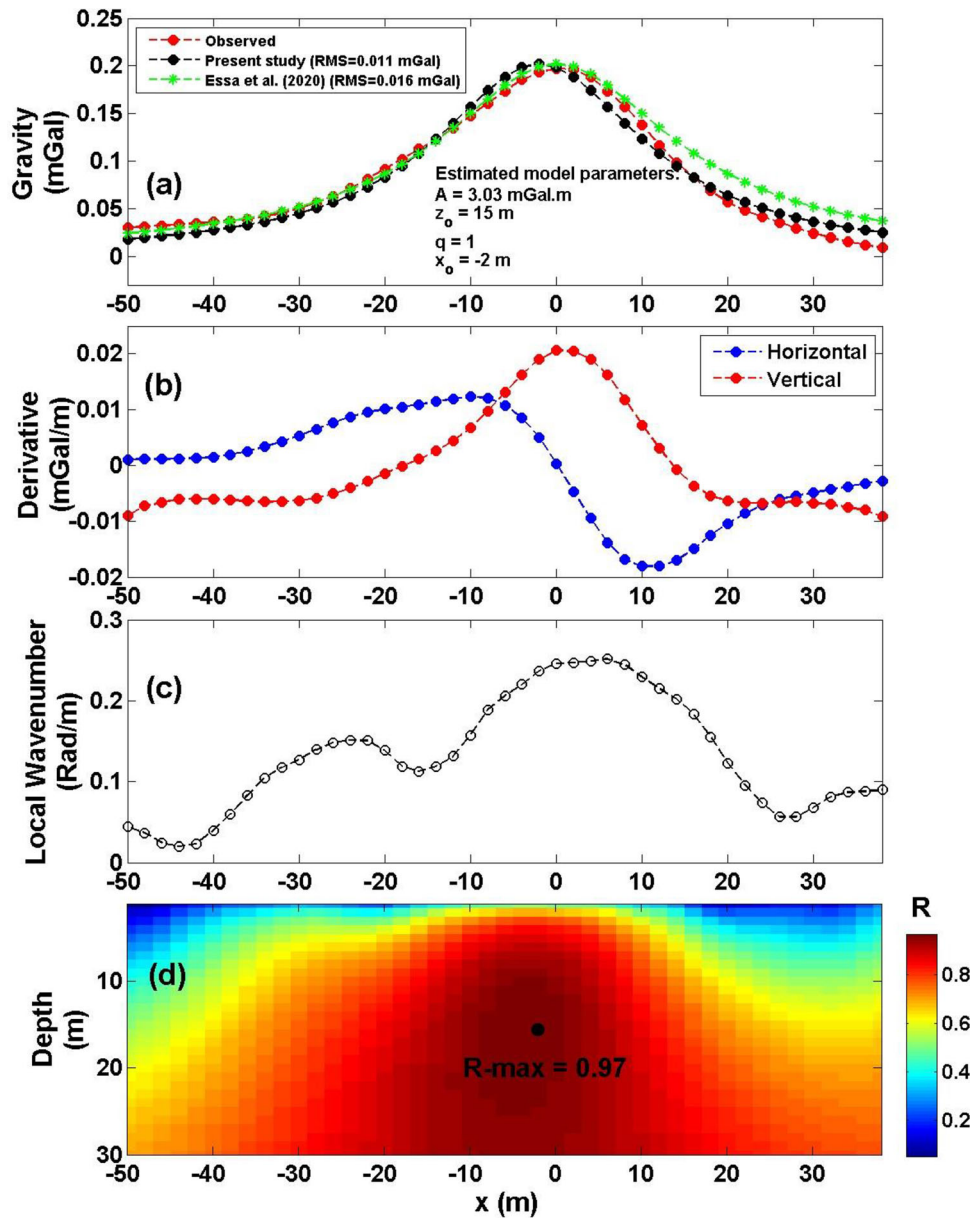
Figure 13. The Camaguey anomaly, Cuba. (**a**) Gravity anomaly profile (red dotted lines) and the best-fitting model (solid black line). (**b**) Horizontal and vertical derivatives of the data shown in (**a**). (**c**) Local wavenumber of the data presented in (**b**). (**d**) R image (maximum $R = 0.97$).

CONCLUSIONS

In this paper, an efficient inversion imaging algorithm was applied to model gravity data caused by different sources (sphere, vertical cylinder, and horizontal cylinder). The algorithm demonstrated here can be used in mineral/ore exploration because it can predict different structure parameters,

Table 10. Maximum R for the various shape factors of the Camaguey anomaly, Cuba

Shape factor (q)	Maximum R
0.5	0.967862
0.6	0.967862
0.7	0.969148
0.8	0.969448
0.9	0.969642
1	**0.969692**
1.1	0.969653
1.2	0.969563
1.3	0.969532
1.4	0.969484
1.5	0.969420

Bold refers to the maximum value overall R

including amplitude factor (A), depth (z_o), body origin (x_o), and shape factor (q), with high accuracy and with no need of a priori information. The suggested algorithm applies the correlation factor (R) between the local wavenumber of the observed gravitational field and that of the computed field. The results show that the maximum R reflects the best-estimated model. In addition, the proposed approach represents an imaging algorithm which offers good and fast (only taking several seconds of) imaging for the subsurface depth and location of hidden anomalous sources. The efficiency, accuracy, and stability of the proposed algorithm were tested by applying it to three different synthetic cases,

Table 11. The recovered parameters for the Camaguey gravity anomaly, Cuba, compared to results in the published literature

Model parameters	Mehanee (2014)	Biswas (2015)	Ekinci et al. (2016)	Essa et al. (2020)	Present study
A (mGal·m)	3	3.5	111.34 (mGal.m^2)	1.86	3.03
z_o (m)	16	16.2	23.23	16	15
q	1.0	1.0	1.5	0.9	1
x_o (m)	–	− 1.8	58.73	0	− 2
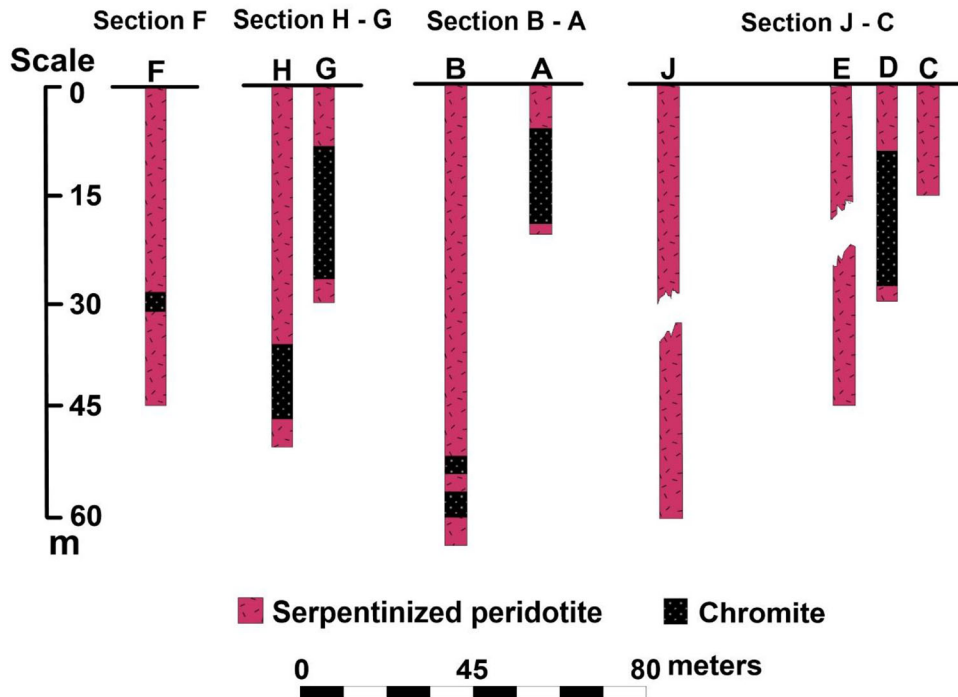
Figure 14. The Camaguey anomaly, Cuba. Drilling information; F, H–G, B–A, and J–C represent labels of drill holes (redrawn from Figure 4 of Davis et al., 1957).
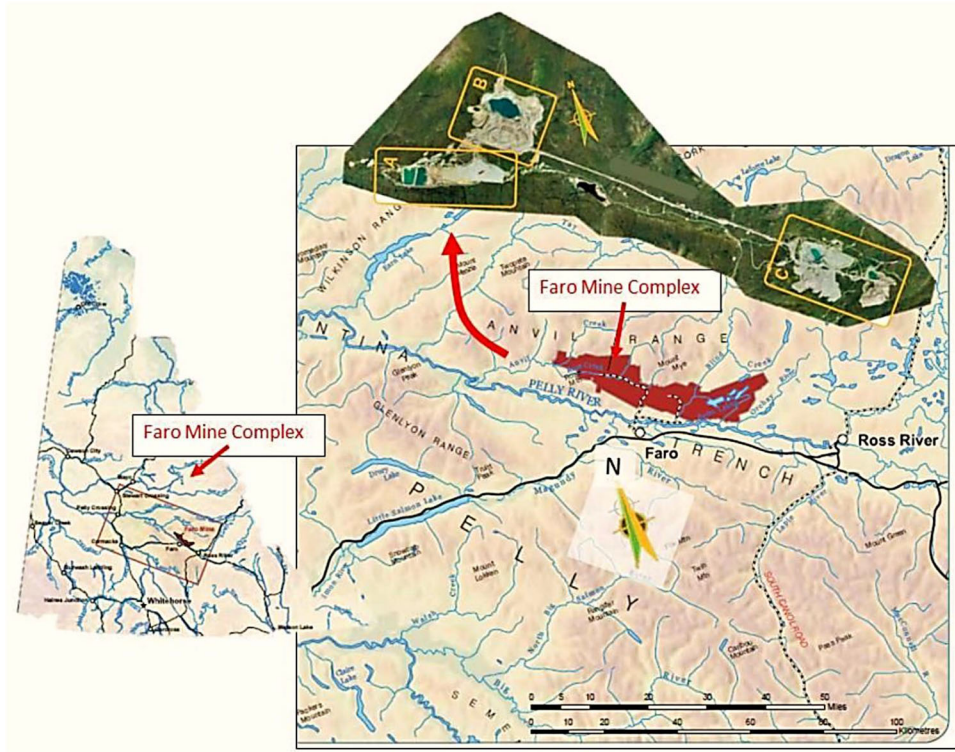
Figure 15. Location map with site layout at the Faro Mine Complex, Canada (from Tang, 2011).
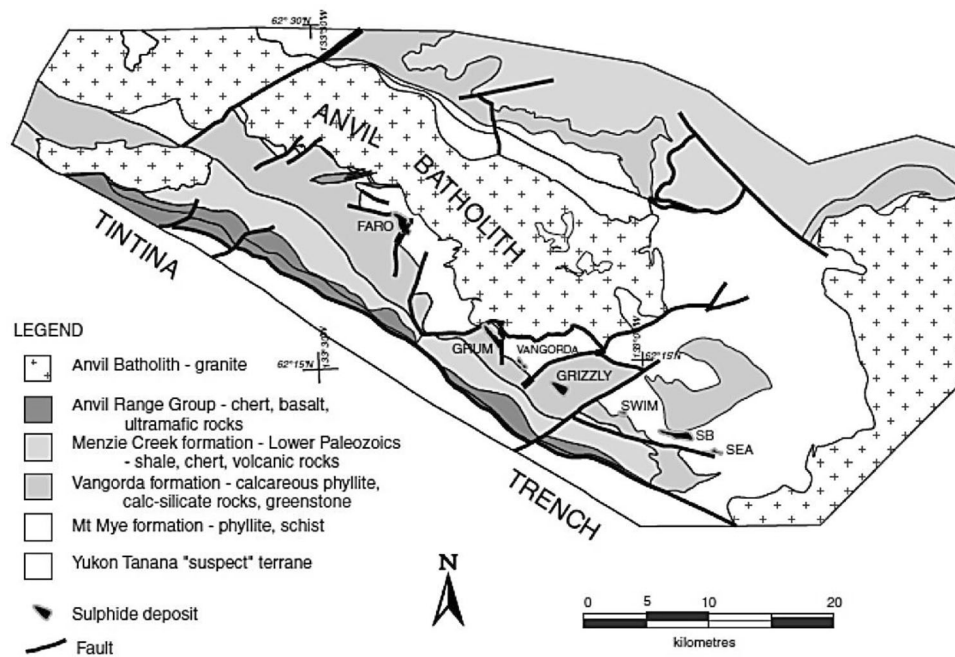

Figure 16. Geology of the Anvil District, Canada (from Tang, 2011). The Faro sulfide deposit is marked at the figure.
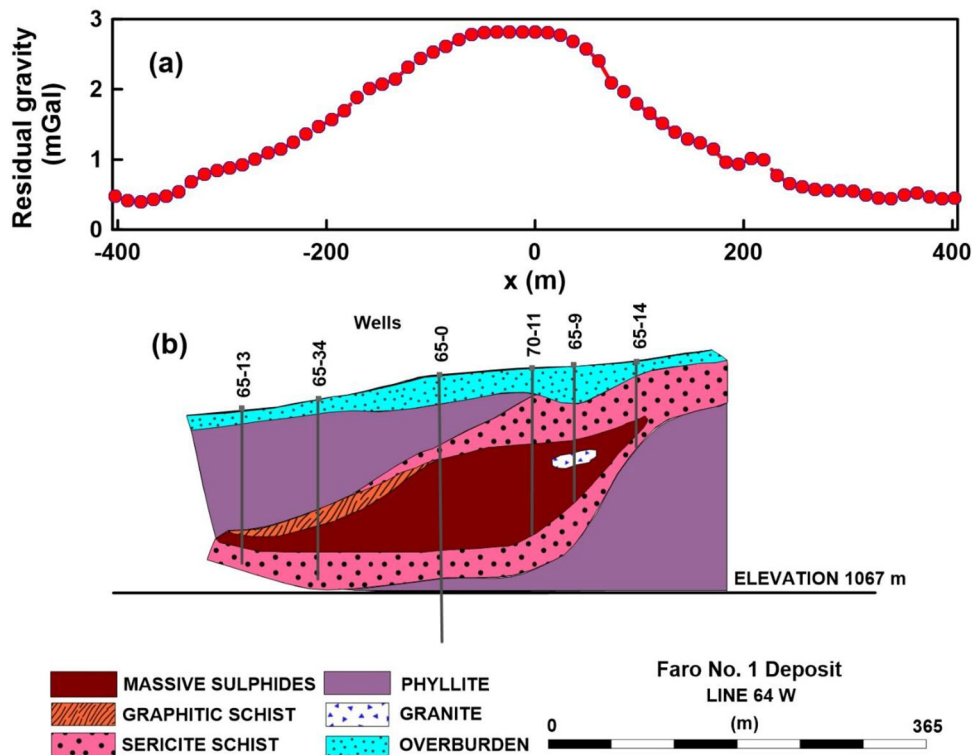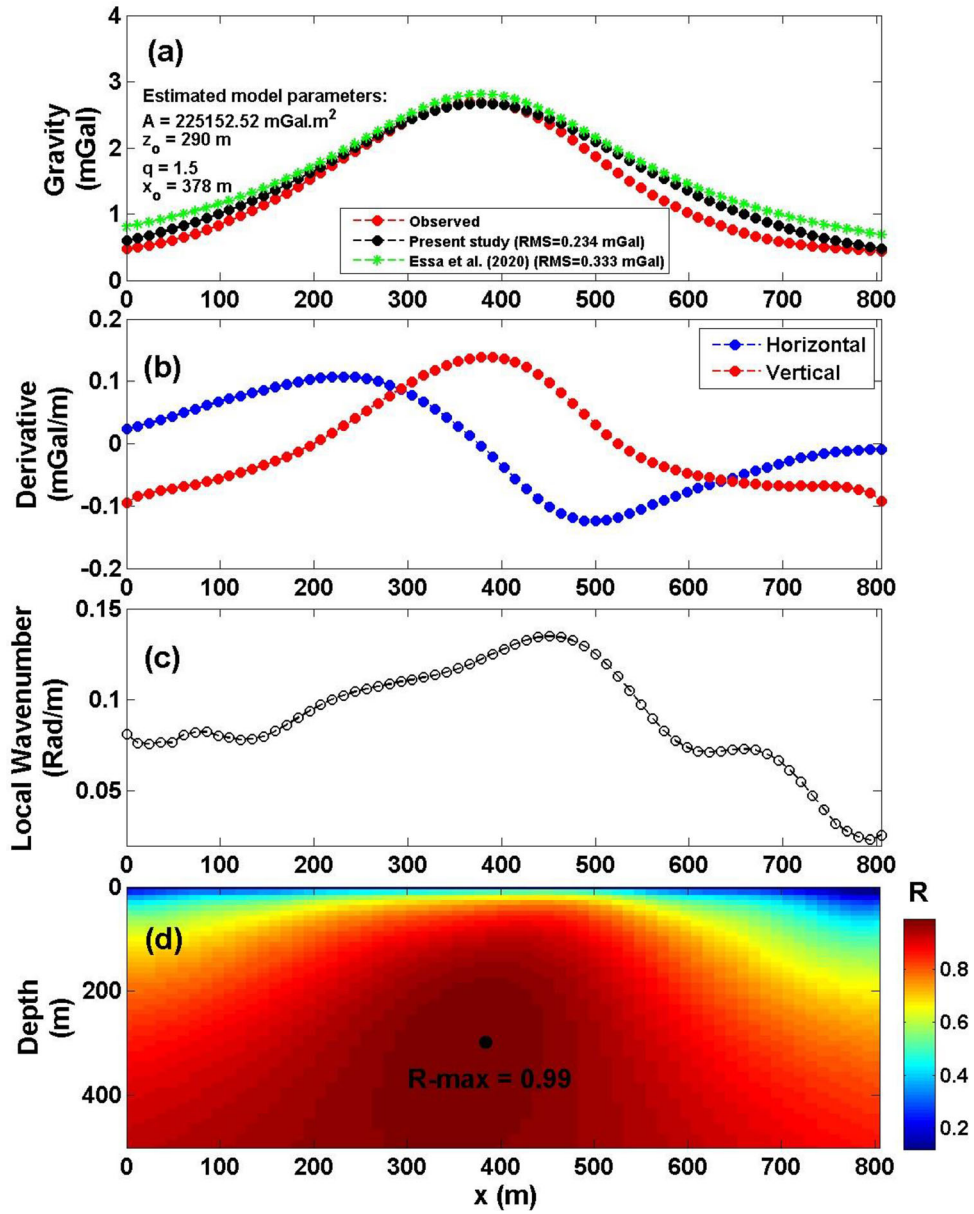
Figure 17. The Faro Pb–Zn anomaly, Yukon, Canada. (**a**) Residual gravity field. (**b**) Geological cross section with boreholes (modified after Brock, 1973).

including a pure example, a noisy example contaminated with different percentages (10% and 20%) of Gaussian random noise (i.e., normal distribution with mean = 0 and standard deviation = 1), and an example with regional background effects. The applicability of the proposed algorithm was checked on three real mineral/ore exploration examples from Canada and Cuba. The resultant models for the real cases correlated very well with drilling data and with different results published in the literature. Finally, from the present study, the proposed algorithm is suitable for mineral/ore deposits exploration, and it is recommended for application to geothermal investigation as well.

Figure 18. The Faro Pb–Zn anomaly, Yukon, Canada. (**a**) Gravity anomaly profile (red dotted lines) and the predicted gravity profile (solid black line). (**b**) Calculated horizontal and vertical derivatives for the profile displayed in (**a**). (**c**) Local wavenumber of the derivatives illustrated in (**b**). (**d**) R image (maximum $R = 0.99$).

Table 12. Maximum R for the various shape factors of the Faro deposit gravity anomaly, Canada

Shape factor (q)	Maximum R
0.5	0.990818
0.6	0.990861
0.7	0.990824
0.8	0.990837
0.9	0.990861
1	0.990900
1.1	0.990937
1.2	0.990954
1.3	0.990995
1.4	0.991023
1.5	**0.991041**

Bold refers to the maximum value overall R

Table 13. Recovered parameters for the Faro deposit gravity anomaly, Canada, compared to results in the published literature

Model parameters	Essa et al. (2020)	Present study
A (mGal·m^{2q-m})	78.6 (mGal.m)	225,152.52 (mGal.m^2)
z_o (m)	195	290
q	0.8	1.5
x_o (m)	371.9	378

ACKNOWLEDGMENTS

FUNDING

DATA AVAILABILITY

The authors declare that the data will be available upon request.

DECLARATIONS

Conflict of Interest There are no financial or nonfinancial interests that are directly or indirectly related to the work submitted for publication.

OPEN ACCESS

REFERENCES

Abdelrahman, E. M., & Essa, K. S. (2015). Three least-squares minimization approaches to interpret gravity data due to dipping faults. *Pure and Applied Geophysics, 172*, 427–438.

Abdelrahman, E. M., & Sharafeldin, S. M. (1995). A least-squares minimization approach to depth determination from numerical horizontal gravity gradients. *Geophysics, 60*, 1259–1260.

Al-Farhan, M., Oskooi, B., Ardestani, V. E., Abedi, M., & Al-Khalidy, A. (2019). Magnetic and gravity signatures of the Kifl oil field in Iraq. *Journal of Petroleum Science and Engineering, 183*, 106397.

Amjadi, A., & Naji, J. (2013). Application of genetic algorithm optimization and least square method for depth determination from residual gravity anomalies. *International Research Journal of Applied and Basic Sciences, 5*, 661–666.

Asfahani, J., & Tlas, M. (2008). An automatic method of direct interpretation of residual gravity anomaly profiles due to spheres and cylinders. *Pure and Applied Geophysics, 165*, 981–994.

Balkaya, C., Ekinci, Y. L., Gokturkler, G., & Turan, S. (2017). 3D non-linear inversion of magnetic anomalies caused by prismatic bodies using differential evolution algorithm. *Journal of Applied Geophysics, 136*, 372–386.

Barrett, T. J., Cattalani, S., Hoy, L., Riopel, J., & Lafleur, P. J. (1992). Massive sulfide deposits of the Noranda area, Quebec. IV. The Mobrun mine. *Canadian Journal of Earth Science, 29*, 1349–1374.

Biswas, A. (2015). Interpretation of residual gravity anomaly caused by a simple shaped body using very fast simulated annealing global optimization. *Geoscience Frontiers, 6*, 875–893. https://doi.org/10.1016/j.gsf.2015.03.001.

Biswas, A. (2016). Interpretation of gravity and magnetic anomaly over thin sheet-type structure using very fast simulated annealing global optimization technique. *Modeling Earth Systems and Environment, 2*, 30.

Biswas, A., Mandal, A., Sharma, S. P., & Mohanty, W. K. (2014). Delineation of subsurface structure using self-potential, gravity and resistivity surveys from South Purulia Shear Zone, India: Implication to uranium mineralization. *Interpretation, 2*, T103–T110.

Biswas, A., Parija, M. P., & Kumar, S. (2017). Global nonlinear optimization for the interpretation of source parameters from total gradient of gravity and magnetic anomalies caused by thin dyke. *Annals of Geophysics, 60*, G0218. https://doi.org/10.4401/Ag-7129.

Braitenberg, C., Sampietro, D., Pivetta, T., Zuliani, D., Barbagallo, A., Fabris, P., Rossi, L., Fabbri, J., & Mansi, A. H. (2016). Gravity for detecting caves: Airborne and terrestrial simulations based on a comprehensive Karstic cave benchmark. *Pure and Applied Geophysics, 173*, 1243–1264.

Brock, J. S. (1973). Geophysical exploration leading to the discovery of the Faro deposit. *Canadian Mining and Metallurgical Bulletin*, *66*(738), 97–116.

Caumartin, C., & Caill, C.M.-F. (1990). Volcanic stratigraphy and structure of the Mobrun mine. In the northwestern Quebec polymetallic belt. Edited by M. Rive, P., Verpaelst, Y., Gagnon, et al. *Canadian Institute of Mining and Metallurgy, 43*, 133–142.

Chai, Y., & Hinze, W. J. (1988). Gravity inversion of an interface above which the density contrast varies exponentially with depth. *Geophysics, 53*, 837–845.

Chen, Y. Q., Zhang, L. N., & Zhao, B. B. (2017). Application of Bi-dimensional empirical mode decomposition (BEMD) modeling for extracting gravity anomaly indicating the ore-controlling geological architectures and granites in the Gejiu tin-copper polymetallic ore field, southwestern China. *Ore Geology Review, 88*, 832–840.

Davis, W. E., Jackson, W. H., & Richter, D. H. (1957). Gravity prospecting for chromite deposits in Camaguey Province, Cuba. *Geophysics, 22*, 848–869.

Di Maio, R., Milano, L., & Piegari, E. (2020). Modeling of magnetic anomalies generated by simple geological structures through genetic-price inversion algorithm. *Physics of the Earth and Planetary Interiors, 305*, 106520.

Di Maio, R., Rani, P., Piegari, E., & Milano, L. (2016). Self-potential data inversion through a genetic-price algorithm. *Computers and Geosciences, 94*, 86–95.

Ekinci, Y. L., Balkaya, C., Gokturkler, G., & Turan, S. (2016). Model parameter estimations from residual gravity anomalies due to simple-shaped sources using Differential Evolution Algorithm. *Journal of Applied Geophysics, 129*, 133–144.

Ekinci, Y. L., Ertekin, C., & Yiğitbas, E. (2013). On the effectiveness of directional derivative based filters on gravity anomalies for source edge approximation: Synthetic simulations and a case study from the Aegean Graben system (western Anatolia, Turkey). *Journal of Geophysics and Engineering, 10*, 035005.

Elawadi, E., Salem, A., & Ushijima, K. (2004). Detection of cavities and tunnels from gravity data using a neural network. *Exploration Geophysics, 32*, 204–208.

Elieff, S., & Sander, S. (2004). AIRGrav Airborne gravity survey in Timmins, Ontario. In *Airborne gravity workshop, ASEG-PESA* (pp. 111–119).

Eshaghzadeh, A., & Hajian, A. (2018). 2D inverse modeling of residual gravity anomalies from Simple geometric shapes using Modular Feed-forward Neural Network. *Annulus Geophysics, 61*, SE115. https://doi.org/10.4401/ag-7540.

Essa, K. S. (2007). A simple formula for shape and depth determination from residual gravity anomalies. *Acta Geophysica, 55*, 182–190.

Essa, K. S. (2011). A new algorithm for gravity or self-potential data interpretation. *Journal of Geophysics and Engineering, 8*, 434–446.

Essa, K. S. (2012). A fast interpretation method for inverse modeling of residual gravity anomalies caused by simple geometry. *Journal of Geological Research, 2012*, 327037.

Essa, K. S. (2013). Gravity interpretation of dipping faults using the variance analysis method. *Journal of Geophysics and Engineering, 10*, 015003.

Essa, K. S. (2014). New fast least-squares algorithm for estimating the best-fitting parameters of some geometric-structures to measured gravity anomalies. *Journal of Advanced Research, 5*, 57–65.

Essa, K. S., & Elhussein, M. (2018). Gravity data interpretation using different new algorithms: A comparative study. *Gravity - Geoscience Applications, Industrial Technology and Quantum Aspect*. https://doi.org/10.5772/intechopen.71086.

Essa, K. S., Mehanee, S. A., Soliman, K. S., & Diab, Z. E. (2020). Gravity profile interpretation using the R-parameter imaging technique with application to ore exploration. *Ore Geology Reviews, 126*, 103695.

Essa, K. S., & Munschy, M. (2019). Gravity data interpretation using the particle swarm optimization method with application to mineral exploration. *Journal of Earth System Science, 128*, 123.

Essa, K. S., Nady, A. G., Mostafa, M. S., & Elhussein, M. (2018). Implementation of potential field data to depict the structural lineaments of the Sinai Peninsula, Egypt. *Journal of African Earth Science, 147*, 43–53.

Ghosh, G. K. (2016). Interpretation of gravity data using 3D Euler deconvolution, tilt angle, horizontal tilt angle and source edge approximation of the North-West Himalaya. *Acta Geophysica, 64*, 1112–1138.

Grant, F. S., & West, G. F. (1965). *Interpretation theory in applied geophysics*. McGraw-Hill Book Co.

Greene, E. F., & Bresnahan, C. M. (1998). Gravity's role in a modern exploration program. In R. I. Gibson & P. S. Millegan (Eds.), *Geologic applications of gravity and magnetic, Case Histories* (pp. 9–12). SEG and AAPG.

Gupta, O. P. (1983). A least-squares approach to depth determination from gravity data. *Geophysics, 48*, 357–360.

Hinze, W. J., Von Frese, R. R. B., & Saad, A. H. (2013). *Gravity and magnetic exploration*. Cambridge University Press.

Jacoby, W., & Smilde, P. L. (2009). *Gravity interpretation, fundamentals and application of gravity inversion and geological interpretation*. Springer.

Kaftan, I. (2017). Interpretation of magnetic anomalies using a genetic algorithm. *Acta Geophysica, 65*, 627–634.

Kara, I., & Kanli, A. I. (2005). Nomograms for interpretation of gravity anomalies of vertical cylinders. *Journal of the Balkan Geophysical Society, 8*, 1–6.

Kearey, P., Brooks, M., & Hill, I. (2002). *An introduction to geophysical exploration*. Blackwell Publishing.

Kumar, K. S., Rajesh, R., & Tiwari, R. K. (2018). Regional and residual gravity anomaly separation using the singular spectrum analysis-based low pass filtering: A case study from Nagpur, Maharashtra, India. *Exploration Geophysics, 49*, 398–408.

Linford, N. (2006). The application of geophysical methods to archaeological prospection. *Reports on Progress in Physics, 69*, 2205–2257.

Ma, G., Liu, C., Xu, J., & Meng, Q. (2017). Correlation imaging method based on local wavenumber for interpreting magnetic data. *Journal of Applied Geophysics, 138*, 17–22.

Mehanee, S. A. (2014). Accurate and efficient regularised inversion approach for the interpretation of isolated gravity anomalies. *Pure and Applied Geophysics*, *171*(8), 1897–1937. https://doi.org/10.1007/s00024-013-0761-z.

Mohan, N. L., Anandababu, L., & Roa, S. (1986). Gravity interpretation using the Melin transform. *Geophysics, 51*, 14–22.

Nabighian, M. N. (1972). The analytic signal of two-dimensional magnetic bodies with polygonal cross-section: Its properties

and use for automated anomaly interpretation. *Geophysics, 37*, 507–517.

Nettleton, L. L. (1976). *Gravity and Magnetics in Oil Prospecting*. McGraw Hill Book Co.

Padín, J., Martín, A., & Anquela, A. B. (2012). Archaeological microgravimetric prospection inside don church (Valencia, Spain). *Journal of Archaeological Science, 39*, 547–554.

Panisova, J., & Pasteka, R. (2009). The use of microgravity technique in archaeology: A case study from the St. Nicolas Church in Pukanec, Slovakia. *Contributions to Geophysics and Geodesy, 39*, 237–254.

Pinto, V., & Casas, A. (1996). An Interactive 2D and 3D gravity modeling program for IBM-compatible personal computers. *Computers and Geosciences, 22*(5), 535–546. https://doi.org/10.1016/0098-3004(95)00125-.

Prakasa Rao, T. K. S., Subrahmanyan, M., & Srikrishna Murthy, A. (1986). Nomograms for direct interpretation of magnetic anomalies due to long horizontal cylinders. *Geophysics, 51*, 2150–2159.

Reynolds, J. M. (1997). *An introduction to applied and environmental geophysics* (p. 796). Wiley.

Roy, L. (2001). Short note: Source geometry identification by simultaneous use of structural index and shape factor. *Geophysical Prospecting*, *49*(1), 159–164. https://doi.org/10.1046/j.1365-2478.2001.00239.x.

Roy, L., Agarwal, B. N. P., & Shaw, R. K. (2000). A new concept in Euler deconvolution of isolated gravity anomalies. *Geophysical Prospecting, 48*, 559–575.

Saad, A. H. (2006). Understanding gravity gradients: A tutorial. *Leading Edge, 25*(8), 942–949.

Salem, A., Ravat, D., Mushayandebvu, M. F., & Ushijima, K. (2004). Linearized least-squares method for interpretation of potential-field data from sources of simple geometry. *Geophysics, 69*, 783–788.

Santana, M. M. U., Moura, M. A., Olivo, G. R., Botelho, N. F., Kyser, T. K., & Bühn, B. (2011). The La Unión Au ± Cu prospect, Camagüey District, Cuba: Fluid inclusion and stable isotope evidence for ore-forming processes. *Mineralium Deposita*, *46*(1), 91–104. https://doi.org/10.1007/s00126-010-0313-8.

Sen, M. K., & Stoffa, P. L. (2013). *Global optimization methods in geophysical inversion* (2nd ed.). Cambridge Publisher.

Siegel, H. O., Winkler, H. A., & Boniwell, J. B. (1957). Discovery of the Mobrun Copper Ltd. sulphide deposit, Noranda Min-ing District, Quebec. In *Methods and case histories in mining geophysics* (pp. 237–245) Commonwealth Mining and Metallurgical Congress 6th, Vancouver.

Singh, A., & Biswas, A. (2016). Application of global particle swarm optimization for inversion of residual gravity anomalies over geological bodies with idealized geometries. *Natural Resources Research, 25*, 297–314.

Sivakumar Sinha, G. D. J., & Ram Babu, H. V. (1985). Analysis of gravity gradients over a thin infinite sheet. *Proceedings of the Indian Academy of Sciences, Earth and Planetary Sciences, 94*, 71–76.

Stavrev, P. Y. (1997). Euler deconvolution using differential similarity transformations of gravity or magnetic anomalies. *Geophysical Prospecting, 45*, 207–246.

Tang, M. S. M. (2011). *Delineation of groundwater capture zone for the Faro mine, Faro mine complex, Yukon territory*. BSc thesis. University of British Columbia, Vancouver, Canada.

Tarantola, A. (2005). *Inverse problem theory and methods for model parameter estimation*. SIAM.

Telford, W. M., Geldart, L. P., & Sheriff, R. E. (1990). *Applied Geophysics*. Cambridge University Press.

Thompson, D. T. (1982). EULDPH—A new technique for making computer-assisted depth estimates from magnetic data. *Geophysics, 47*, 31–37.

Toushmalani, R. (2013). Comparison result of inversion of gravity data of a fault by particle swarm optimization and Levenberg-Marquardt methods. *SpringerPlus, 2*, 462.

Werner, S. (1953). *Interpretation of magnetic anomalies at sheet-like bodies Sveriges Geologiska Undersok*. Ser CC Arsbok 43 No 6.

Wu, G. J., Liu, H., Zou, Z. B., Yang, G. L., & Shen, C. Y. (2014). 3-Dimensional inversion for gravity anomaly calculation in complex geologic region. *Advanced Materials Research, 962–965*, 238–241.

Zhang, C., Mushayandebvu, M. F., Reid, A. B., Fairhead, J. D., & Odegard, M. E. (2000). Euler deconvolution of gravity tensor gradient data. *Geophysics, 65*, 512–520.

Zhang, J., Zhong, B., Zhou, X., & Dai, Y. (2001). Gravity anomalies of 2-D bodies with variable density contrast. *Geophysics, 66*, 809–813.

Zhdanov, M. S. (2002). *Geophysical inversion theory and regularization problems*. Elsevier.